Author Manuscript

Author Manuscript

Author Manuscript

Author Manuscript

HHS Public Access

Author manuscript

J Inorg Biochem. Author manuscript; available in PMC 2017 February 01.

Published in final edited form as:

J Inorg Biochem. 2016 February ; 155: 44–55. doi:10.1016/j.jinorgbio.2015.11.001.

Cytochrome Unfolding Pathways from Computational Analysis of Crystal Structures

John J. Kozak[a], **Harry B. Gray**[b], and **Roberto A. Garza-López**[c,*]

[a]DePaul University, 243 South Wabash Ave. Chicago IL 60604-6116

[b]Beckman Institute, California Institute of Technology, Pasadena CA 91125

[c]Department of Chemistry and Seaver Chemistry Laboratory, Pomona College, Claremont CA 91711

Abstract

We have developed a model to study the role of geometrical factors in influencing the early stages of unfolding in three cytochromes: cyt *c*′, cyt *c*-b_{562} and cyt *c*. Each stage in unfolding is quantified by the spatial extension $\langle \hat{\lambda_i} \rangle$ of n-residue segments, and by their angular extension $\langle \beta_n \rangle$. Similarities and differences between and among the three cytochromes in the unfolding of helical and non-helical regions can be determined by analyzing the data for each signature separately. Definite conclusions can be drawn when spatial and angular changes are considered in tandem. To facilitate comparisons, we present graphical portraits of the three cytochromes at the same stage of unfolding, and in relation to their native state structures. We also display specific segments at different stages of unfolding to illustrate differences in stability of defined domains thereby allowing us to make specific predictions on the unfolding of corresponding internal and terminal helices in cyt *c*′ and cyt *c*-b_{562}. Our work accords with an earlier experimental report on the presence and persistence of a hydrophobic core in cyt *c*.

GRAPHICAL ABSTRACT (SYNOPSIS)

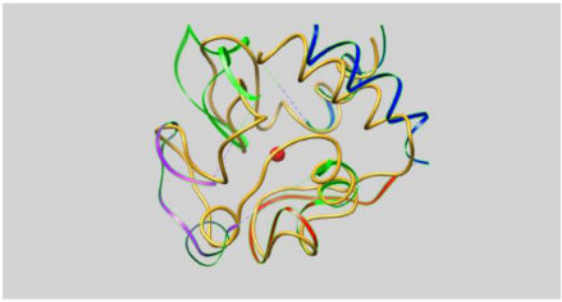

Native (goldenrod) and second extended state for cyt c.

*rgarza@pomona.edu. Fax: 909-607-9621.

Publisher's Disclaimer: This is a PDF file of an unedited manuscript that has been accepted for publication. As a service to our customers we are providing this early version of the manuscript. The manuscript will undergo copyediting, typesetting, and review of the resulting proof before it is published in its final citable form. Please note that during the production process errors may be discovered which could affect the content, and all legal disclaimers that apply to the journal pertain.

Author Manuscript Author Manuscript Author Manuscript Author Manuscript

The N-terminal and C-terminal α-helices are in blue, the green loop and the green α-helix are in green, the infrared loop is in magenta, and the red loop in red.

I. Introduction

Both electrostatic and hydrophobic forces play key roles in controlling polypeptide flow up and down a folding funnel [1]. Experimental [2–9] and theoretical [10–13] investigations support the existence of a multiplicity of populations of unfolded configurations, both compact and extended, in denatured ensembles. Funneled energetics of the landscape are believed to be important in influencing unfolded ensembles in the denatured state. But questions remain on whether the folding of small proteins occurs via a hierarchical or non-hierarchical mechanism [14–22], i.e., whether native-like secondary structures form rapidly, interacting with each other to produce intermediates of ever-increasing complexity, or whether folding can be envisioned as a two-state process with no intermediate states.

To provide insight, some workers have focused on early stages in the denaturation, arguing that unfolding is the reverse of folding. Prominent among these efforts are the primarily theoretical and computational studies of Lazaradus and Karplus [23], and Guzzi, Sportelli et al. [24–28], as well as the experimental work of Englander et al. [29] on cytochrome *c*, and Michel and Bren on cytochrome *c*-551 [30]. In an early application of our geometrical model, we found substantial agreement between the unfolding behavior of distinct regions in cyt *c* (foldons) identified in [29] and the predictions of our model, and this will be documented further in the present study.

The stability of a thermodynamic phase can be disrupted not only by changes in such extensive variables as temperature and pressure, but also by local perturbations arising from spontaneous fluctuations. An infinitesimal change in these variables can induce an instability, and may result in transition to a different phase. In our analysis, we take as the starting point the thermodynamically stable state of a protein as defined by its crystallographic structure. Importantly, this is an optimized structure determined by the entire free energy landscape; all inter-residue contacts in the folded protein are encoded (exactly). To visualize *early* stages in protein denaturation, we have developed a geometrical model to “track” the consequences of perturbing the (already optimized) structure of a protein in its native state.

In formulating our approach, we have been guided by the seminal contributions of Ramachandran [31]. He and his coworkers used crystallographic coordinates to identify two dihedral angles $\{\phi, \psi\}$ flanking each peptide bond, and constructed $\{\phi, \psi\}$ plots for all residues in a given protein. From these plots, theoretically favored regions (conformations of the native state) could be established from geometrical arguments alone. Our “extended Ramachandran” model is similar in spirit, and focuses on the geometrical (steric) factors at play as the native structure of a protein is disrupted and the polypeptide chain begins to unfold.

A fundamental feature of our model is that we keep intact *nearest*-neighbor repulsive *and* attractive interactions between residue *i* and its two nearest-neighbors by introducing a

Author Manuscript Author Manuscript Author Manuscript Author Manuscript

triplet modular unit centered on residue *i*; crystallographic data are used to specify the geometry of this triplet of residues. Perturbations are then introduced by relaxing incrementally steric constraints (only) between and among *non*-nearest neighbor residues of the polypeptide chain. We follow quantitatively (via the direct application of classical Euclidian geometry) the consequences of chain unfolding. A series of n = 5 residue, n = 7 residue, …, n = 15 residue "snapshots" are taken of the changing environment of each residue as the polypeptide chain unfolds; as noted above, the geometry of each triplet, a module of n = 3 residues, is conserved and determined by the native state crystallographic data.

Each stage in unfolding is quantified by two principal signatures: the spatial extension λ_i of a given residue *i* in a n-residue segment and the angular extension β_n of this segment relative to a fixed point. The calculation of these signatures using our geometrical approach was described in a recent series of papers on the unfolding of azurin [32–34]; see also references cited therein. In this study, we use these signatures to compare and contrast the early stages of unfolding in *Rhodopseudomonas palustris* cytochrome *c*′ (cyt *c*′) [35], *E. coli* cytochrome b_{562} (cyt *c*-b_{562}) [36], and yeast iso-1-cytochrome *c* (cyt *c*) [37].

II. Methods

We outline below calculation of the extension metric λ_i and the angular extension β_n using a specific example: the second (n = 7) stage of unfolding for residue *i* in a seven residue segment of cyt *c*′, a protein with 123 residues [35]. In this example below, residue *i* is the central residue in the segment spanning residues *i* = 1 thru *i* = 7. The local environment of residue *i* = 4 is then defined by three adjacent triplets, with each triplet's geometry determined by the native-state crystallographic data. See Fig. (1).

To apply our method, we must first specify the origin of the coordinate system, a fixed point relative to which the unfolding is calculated. In our previous studies on azurin [32–34], the metal ion Cu(II) was assigned as the invariant site; for the three cytochromes studied here, the natural choice is the metal ion Fe(III).

Referring to Fig. (1), the following distances can be calculated from the crystallographic data (Theorem of Pythagoras):

$$\mathrm{D(Fe\,to\,R_{01})}=22.25\ \text{Å};\quad \mathrm{D(Fe\,to\,R_{07})}=13.11\ \text{Å};\quad \mathrm{D(R_{01}\,to\,R_{07})}=11.72\ \text{Å}.$$

Using the Law of Cosines (Proposition 12 in Euclid's *Geometry*) the following angles can be calculated:

$$\beta=24.83^0;\quad \alpha=127.16^0;\quad \gamma=28.01^0.$$

As must be the case, these three angles sum to 180°.

In the fully-extended configuration displayed in Fig. (1), the distance T_{04} can be determined from the crystallographic data:

Author Manuscript Author Manuscript Author Manuscript Author Manuscript

$$T_{04}=R_{01}\,to\,R_{03}+R_{03}\,to\,R_{05}+R_{05}\,to\,R_{07}=19.45\ \text{Å}.$$

Then, using the Law of Sines, we obtain directly the extension metric λ_4 which specifies, for the second stage of unfolding, the change in the radial distance ρ_4' of residue i = 4 from the Fe atom relative to the distance ρ_4 characterizing the native state; here,

$$\rho_4{}'/\rho_4=\lambda_4 \quad \text{with} \quad \lambda_4=1.097.$$

As must be the case, this value can be determined using the Law of Sines and either pair of angles (α, β) or (γ, β).

Again using the crystallographic data and the Law of Cosines, we can determine the angle between residues 1 and 3, residues 3 and 5, and residues 5 and 7:

$$\beta(1\,to\,3)=16.14^0; \quad \beta(3\,to\,5)=7.33^0;\ \beta(5\,to\,7)=24.07^0.$$

The sum of these three angles, characterizing the angular extension of a fully-extended chain centered on residue 4, is 47.54°, a value that can be compared with the angular extension between residues 1 and 7 in the native state as calculated directly from the crystallographic data, viz., β(1 *to* 7) = 24.83°. As expected, the angular extension of the extended state (the linear combination of the above three triplets) is greater than that of the native state (in this case, by a factor of ~ 1.9).

Whereas the above calculation was for a segment centered on residue 4, the crystallographic data can also be used to calculate angular signatures for a *sequence* of residues, for example, valine, isoleucine, alanine and glutamine in Fig. (1). The first sum below is a linear combination of the angles defining n=3 (triplet) segments, and the second is a linear combination of the angles defining n=7 segments, each term centered on one of the residues in the sequence.

$$\sum(n=3)=\beta(3\,to\,5)+\beta(4\,to\,6)+\beta(5\,to\,7)+\beta(6\,to\,8)=7.33^0+20.93^0+24.07^0+19.40^0=71.73^0$$
$$\sum(n=7)=\beta(1\,to\,7)+\beta(2\,to\,8)+\beta(3\,to\,9)+\beta(4\,to\,10)=24.83^0+12.52^0+21.55^0+40.56^0=99.46^0$$

Using these sums, we construct the following ratio:

$$\langle\beta_4\rangle=\sum(n=7)\Big/\sum(n=3)=1.39$$

This ratio provides *one* measure of the change in angular constraints as the local neighborhood of each residue is extended. This measure is not unique. Because our modular unit is a triplet, the angular signature introduced leads to register differences for segments with an even number of residues. The difficulty can be removed in the above signature by

Author Manuscript Author Manuscript Author Manuscript Author Manuscript

introducing an additional (but arbitrary) convention, but this can be avoided altogether by calculating the sums $\Sigma(n = 3)$ and $\Sigma(n = 7)$ as defined above. The advantage gained is that ratios $\langle\beta_n\rangle$ calculated for segments having either an even or odd number of residues can then be compared unambiguously.

To complete the specification of our geometrical model, we recall that one of the diagnostics used to assess the crystallographic data describing a given protein is the α-carbon to α-carbon distance between adjacent residues in the polypeptide chain. For example, averaging over all residues, we calculate this distance to be 3.80 Å for the 123 residues in cyt *c′* [35], 3.83 Å for the 106 residues in cyt *c*-b_{562} [36], and 3.87 Å for the 103 residues in cyt *c* [37]. In the unfolded states which follow from application of our geometrical model, nearest-neighbor α-carbon to α-carbon distances have a larger dispersion about the theoretical 3.80 Å than the native state. Rather than adjust the individual residue-to-residue distances to the value 3.80 Å, we adopt a statistical constraint: the (overall) average α-carbon to α-carbon distance for (all) nearest-neighbor residues for each segment in the polypeptide chain is adjusted to be 3.80 Å (at each stage of unfolding). The adjusted values of λ_i will be denoted $\hat{\lambda_i}$.

Analysis of the crystallographic data for individual cytochromes leads to the identification of distinct regions, e.g., *α*-helices, *β*-sheets, (primarily) hydrophobic regions and turning loops. The full data set for our calculations of the average spatial extension (relative to metal ion), and the average angular extension (relative to the native state) for specific regions of each cytochrome in the first six stages of unfolding is given in the Appendix. Tables A1(a–c) give the $\langle\hat{\lambda_i}\rangle$ values for cyt *c′*, cyt *c*-b_{562}, and cyt *c*; a similar compilation for the $\langle\beta_n\rangle$ is given in Tables A2(a–c).

III. Results

Before presenting our results on the unfolding of individual segments of each cytochrome, we display in Figs. (2–4) the overall (all-residue) portraits of cyt *c′*, cyt *c*-b_{562} and cyt *c* in the second (n = 7) stage of unfolding. To facilitate later comparisons, the residues defining the helical and non-helical regions in each cytochrome are specified in Table 1. The helix H_1 in the two cytochromes, cyt *c′* and cyt *c*-b_{562}, is color coded the same (with a similar convention for the other helices H_2, H_3 and H_4). For cyt *c*, we use the color convention for the foldon regions identified by Englander et al.; see Table 1 in Ref. (29) for specification of five foldon regions in oxidized cyt c. In Figs (2–4) the iron atom is coded in red, the native state is coded in goldenrod, the N-terminal “end” of the polypeptide chain (or region) is coded in magenta, and the C-terminal “end” in cyan. Panels (4a–4h) in Fig. (4) display individual (foldon) regions in cyt *c*.

The portraits, Figs. (2–4), were developed after adjusting the spatial metric λ_i (to $\hat{\lambda_i}$) to ensure that the average α-carbon to α-carbon distance of (all) adjacent residues in the polypeptide chain is 3.80 Å; at this stage of unfolding (and most others), the overall scaling factor is the same for all three cytochromes. The scaling factor for individual segments can be different from that for the protein as a whole; in Tables A1 (a,b,c) we include the scaling factor for distinct helical and non-helical regions in the three cytochromes.

Author Manuscript Author Manuscript Author Manuscript Author Manuscript

Accompanying each portrait is a bar graph which shows the extension $\hat{\lambda_i}$ as a function of residue number for each cytochrome. Similar diagrams were developed in our earlier studies of these cytochromes [38–40], but these were based on calculated values of the (unadjusted) metric λ_i. An advantage of enforcing the constraint on adjacent α-carbon distances is that the resulting data set $\{\hat{\lambda_i}\}$ for residues in a well-defined segment (helical or turning region) is more regular (less punctuated by outliers) than is the case for the original data set $\{\lambda_i\}$.

A. Cytochrome *c′*

We report first results on averages of the spatial and angular signatures for individual segments in cyt *c′*; see Tables A1(a) and A2(a). In the first stage of unfolding, n=5, the first residue for which calculations can be carried out using our geometrical model is $i = 3$, the center residue in the 5-residue segment, residues 1 to 5. In the second stage, n=7, the first residue that can be considered is $i = 4$ [see Fig. (1) and the example in the previous section], …, and for n=15, it is residue $i = 8$. A similar situation pertains when considering residues at the C-terminal end of the polypeptide chain. This attenuation is accompanied by a decrease in angle between terminal residues in the (truncated) segments H_1 and H_4 as the protein unfolds [see Tables A2 (a,b,c)]. Consequently, in following the unfolding, stage by stage, the data set for the terminal helices H_1 and H_4 in cyt c′ is less complete than for the two interior helices, H_2 and H_3. Trends reported for interior helices H_2 and H_3 are more reliable than those for the terminal helices H_1 and H_4.

Conclusions drawn from calculations of regional averages for the spatial and angular signatures are more reliable the longer the segment. In cyt *c′*, the helical region H_1 has 23 residues, H_2 has 27 residues, H_3 has 28 residues, and H_4 has 21 residues. However, the non-helical region K, which is bracketed by the two interior helices, H_2 and H_3, has only 7 residues, so the trends reported for the latter stages of unfolding of this region are less reliable.

Mindful of the above caveats, our calculations show that in the earliest stage of unfolding, n =5, the spatial extension of three of the four helices [H_1, H_3, H_4] is greater than that of both helix H_2 and the non-helical, turning region K. However, in the most extended states, there is a reversal of behavior. The data show that the non-helical region is more extended than either of the two interior helical regions, H_2 and H_3, and for the terminal helices as well.

Turning next to the *angular* signature of segments [H_1, H_2, K, H_3, H_4] in cyt *c′*, we report the ratios $\langle\beta_n\rangle$ in Table A2(a); also included, for comparison, is the angle between the terminal residues of each segment in the native state. In the earliest stage of unfolding, the non-helical segment is more extended than any of the helices. As the protein continues to unfold, the $\langle\beta_n\rangle$ for all four helices increases, whereas the ratio $\langle\beta_n\rangle$ for non-helical region remains relatively constant. In the last stage of unfolding (considered in this study), the $\langle\beta_n\rangle$ ratios suggest that the non-helical, primarily hydrophobic, segment is relatively more compact than the four helical regions.

Author Manuscript Author Manuscript Author Manuscript Author Manuscript

B. Cytochrome *c*-b_{562}

We next report results on the spatial and angular signatures of segments in cyt *c*-b_{562}; see Tables A1(b) and A2(b). Here, helical region H_1 has 16 residues, H_2 has 16 residues, H_3 has 24 residues, and H_4 has 19 residues; the non-helical, turning region in cyt *c*-b_{562} has 14 residues, a factor of two larger than for cyt *c*′.

In contrast to the behavior exhibited by cyt *c*′, no significant differences in spatial extension are found among the four helices in the first stage of unfolding. Also in contrast to the behavior noted for cyt *c*′, the spatial extensions of all four helices {H_1, H_2, H_3, H_4} are smaller than that of the non-helical region, K. However, in the last stage of unfolding, the behavior of the two cytochromes, cyt *c*′ and cyt *c*-b_{562}, is similar; the non-helical region is more extended than the four helical regions.

With respect to the angular signature, the data in Table A2(b) show that in the first stage of unfolding, the $\langle \beta_n \rangle$ for helix H_4 and the non-helical region are comparable and larger than for helices H_1, H_2, and H_3. Significantly, the ratios $\langle \beta_n \rangle$ for the non-helical region increase more gradually in intermediate stages of unfolding than for the helical segments. In the most extended stage, both the terminal helical regions, H_1 and H_4, and the non-helical region, are more compact than the interior helices, H_2 and H_3.

C. Cytochrome *c*

For the articulated protein cyt *c*, data on the spatial metric in Table A1(c) and the angular ratio in Table A2(c) are displayed for the foldon regions identified by Englander et al. [Refs. (21, 29, 41)]. We have obtained results for the N-terminal blue α-helix, the green loop (residues 19–36), the green α-helix (residues 62–70), the infrared loop (residues 40–57), the red loop (residues 71–85) and the C-terminal blue α-helix. Calculations were not done for the yellow β-sheet (the two anti-parallel β-strands, residues 37–39 and 58–61) since application of our geometrical model requires a minimum of n=5 residues.

From their experimental studies on hydrogen exchange of marker residues, Englander et al. deduce that cyt *c* unfolds sequentially as follows:

$$\mathrm{IRYGB\,(Native)} \leftrightarrow \begin{matrix} \mathrm{iRYGB} \\ \\ \mathrm{IrYGB} \end{matrix} \leftrightarrow \mathrm{irYBG} \leftrightarrow \mathrm{iryGB} \leftrightarrow \mathrm{irygB} \leftrightarrow \mathrm{irygb}$$

(in their notation, I represents the infrared loop, R the red loop, Y the anti-parallel β-strand, G the green α-helix, and B the N- and C-terminal α–helices; native state is upper case, unfolded state is lower case). In broad outline, Englander et al. determined that the three helical regions lagged behind the green, red and infrared loops as the protein denatured.

Examining the spatial signatures in Table A3(c), in the first stage of unfolding the results are mixed. The C-terminal blue helix lags behind the green α-helix and the N-terminal blue helix. Values of $\langle \hat{\lambda_i} \rangle$ for the green, infrared and red loops are intermediate between those calculated for the two terminal helices. In the most extended stage of unfolding considered in this study (n = 15), the spatial extensions of the helical and non-helical regions follow the

Author Manuscript Author Manuscript Author Manuscript Author Manuscript

order reported by Englander et al. *except* that the order of the infrared loop and the red loop are reversed. The infrared loop is bracketed by the two β-strands; in our model the influence of the β-strands cannot be decoupled from the behavior of adjacent residues in the infrared loop. This limitation may account for the reversal.

From the angular signatures $\langle\beta_n\rangle$ reported in Table A2(c), we find that in the first stage of unfolding, the three helical regions are more compact than the three non-helical loops. In the most unfolded stage (n = 15), the green loop and the red loop are more compact than the N-terminal blue helix, the green helix and the C-terminal blue helix. As noted above, values calculated for $\langle\beta_n\rangle$ for the infrared loop (may) reflect the fact that this region is bracketed by the two β-strands.

IV. Discussion

The principal conclusion that can be drawn from our study is that although the first stages of unfolding of cyt *c*′, cyt *c*-b_{562} and cyt *c* have some features in common, data on the spatial and angular signatures of specific regions reveal quantitative, and sometimes qualitative, differences in behavior. We have drawn attention to factors that may limit the reliability of our analysis. Apart from these, no further approximations are introduced in calculating values of the spatial and angular signatures. The only functions required to elaborate our geometrical model are sines and cosines, and the trigonometric relations that these functions satisfy. Since our geometrical model is strictly deterministic and based on well-defined functions, no technical restrictions (e.g., software limitations or compilation times) arise in carrying out calculations. The task then becomes one of analyzing what these data are telling us.

Displaying calculated values of $\hat{\lambda_i}$ and β_n may be viewed as projections of the underlying crystallographic data set on different screens to illuminate facets of the protein's structure as it unfolds. For example, as noted in the previous section, in the earliest stage of unfolding, the spatial signature of the internal helix H_2 in cyt *c*-b_{562} suggests that this helix (with 16 residues, 4 turns of α-helix) is only slightly displaced from its native state configuration, whereas H_2 in cyt *c*′ (27 residues and 7 turns) shows a more pronounced departure. This is somewhat counterintuitive; but, since H_2 is an internal helix in both cytochromes, and both helices have at least 4 turns, neither of the caveats mentioned previously apply. We can be reasonably confident that there are real differences in the unfolding behavior of H_2 in the two cytochromes.

This conclusion is based on examining data on both the spatial signature and angular signature, but *independently*. In fact, as the protein unfolds, both spatial and angular extensions of the polypeptide chain occur *synchronously*. Hence, it is desirable to visualize the unfolding when both diagnostics are at play, concurrently. The conformational changes in helix H_2 in the first two stages (n = 5, 7) of unfolding are displayed graphically in Fig. 5 for cyt *c*-b_{562} and in Fig. 6 for cyt *c*′. These graphics substantiate the conclusion reached above: in early stages of unfolding, the behavior of the internal helix H_2 is qualitatively different in the two cytochromes, with the helix H_2 in cyt *c*′ being more labile.

Author Manuscript Author Manuscript Author Manuscript Author Manuscript

As noted in the Introduction, the present study has been guided by Ramachandran's recognition of the importance of geometrical (steric) constraints in delimiting regions of the (ϕ, ψ) phase portrait. In Figs. (7,8) we display the Ramachandran plot for cyt c' and cyt *c*-b_{562}, respectively, color coded so that the residue coordinates for helix H_2 can be distinguished. The phase portrait for cyt *c*-b_{562} is relatively localized, whereas the distribution of H_2 residues in cyt c' is (much) more delocalized. Importantly, we see that the different lability of the H_2 helices in the two cytochromes is already forecast in the (ϕ, ψ) phase portrait of the native state of each. This correspondence may be an isolated, accidental correlation, but if the correlation can be shown to be more general, then it opens up a new pathway for using native state, (ϕ, ψ) phase portraits in concert with our geometrical approach to identify regions of a given protein that are more likely to destabilize as the polypeptide begins to denature.

The angular signatures for the two internal helices H_2 and H_3 of cyt c' and cyt *c*-b_{562}, show a significant change from the early to the latter stages of unfolding. The non-helical region region in cyt c' (residues 61 to 67) is probably too small to draw meaningful conclusions from the data. This is not the case for cyt *c*-b_{562} for which the non-helical region spans 14 residues, a length which is comparable to the adjacent internal helices, H_2 and H_3. The data for this segment show that the angular signature remains effectively constant as the protein unfolds, i.e., the turning region remains relatively intact. This suggests that the region contains a "hydrophobic core" which is conserved in the early stages of denaturation.

Lastly, we consider the results for cyt *c*. This protein provides an "acid test" for the usefulness of the geometrical model described here because, in contrast to cyt c' and cyt *c*-b_{562}, there are two lines of experimental evidence on the site-specific or regional behavior of cyt *c* as this protein unfolds. In addition to the experimental studies of Englander et al. (21,29,41) on hydrogen exchange of marker residues in horse heart cyt c, we have for yeast *iso*-1 cytochrome c the results of a study [9] of the time-resolved fluorescence energy transfer (trFET) from a dansyl fluorophore (Dns) to Fe (III). The derivatized residues examined in the trFET experiments [9] are in correspondence with residue "markers" used in (21,29) for hydrogen exchange studies.

The trFET study revealed large populations of compact structures in the unfolded Dns(C50), Dns(C39) and Dns(C66) proteins. Interestingly, Pletneva et al. [9] suggested that the associated compact structures play a role in forming a hydrophobic core during the folding process. Whereas residue 39 is adjacent to one of the β-strands, and residue 85 is adjacent to the C-terminal blue helix, residue 50 is in the middle of the infrared loop, a segment with 17 residues, and hence a region where we can expect our geometrical model to yield reliable predictions.

As with the helices, while the individual spatial and angular signatures are of value in analyzing the behavior of the infrared loop on unfolding, a composite portrait when both factors are at play is more instructive. Displayed in Fig. 9a is the behavior of this non-helical region in the first stage of unfolding (n = 5), and in Fig. 9b an intermediate stage (n = 9) and the last stage considered in this study (n=15). Focusing on the interior of the region, in the vicinity of residue 50, proximity to the native state configuration is displayed in both stages

Author Manuscript Author Manuscript Author Manuscript Author Manuscript

of unfolding. This strongly suggests the presence and persistence of a hydrophobic core, in agreement with the analysis in [9].

V. Conclusions

The signatures $\{\lambda_i, \hat{\beta}_n\}$ describe the unfolding of cyt *c*′, cyt *c*-b_{562}, and cyt *c*. From these results as well as from those obtained in our recent study of several azurins [32–34], the importance of geometrical factors in influencing the early stages of denaturation has been established. Whereas the summative portraits presented in Tables A1(a,b,c) and Tables A2(a,b,c) present quantitative evidence on the separate, spatial and angular behavior of specific regions, the graphical representations in the figures present an integrated picture of the unfolding and allow more definite predictions to be made.

We note that in the azurin studies [32–34] a third signature was introduced, one that allowed conclusions to be drawn on segmental chain motion. A systematic study of this signature for cyt *c*′, cyt *c*-b_{562}, and cyt *c* will be presented in a separate contribution, and will be accompanied by molecular dynamics evidence.

Importantly, we have identified regions in the protein where structures are perturbed from ones they would adopt if they were not embedded in a globally minimized framework. The beauty of our model is its simplicity: as in Ramachanran's use of crystallographic coordinates to identify the dihedral angles $\{\phi, \psi\}$, all you need in our geometrical approach to predict unfolding propensities are the atom coordinates of a good crystal structure.

Acknowledgments

We wish to acknowledge conversations with a number of colleagues who have provided valuable insights on both the strengths and limitations of the model presented here. Special thanks go to David Eisenberg, who suggested that the development would benefit from a graphical representation of selected results, and to J.R. Winkler. The authors would also like to thank one of the reviewers for drawing attention to one aspect of Ramachandran's (ϕ, ψ) plots. Financial support for R.A.G.-L. was provided by the Howard Hughes Medical Institute Research Program from Pomona College. The authors would like to thank Pomona College undergraduates Sabari Kumar, Don Chen, Spencer Satz and Neil Chan for their help in getting the images for this paper. The molecular graphics images were produced using the Chimera package from the Computer Graphics Laboratory, University of California, San Francisco (supported by NIH P41 RR-01081). H.B. Gray thanks NIH (DK019038) and the Arnold and Mabel Beckman Foundation for support of the work.

References

1. Weinkam P, Pletneva EV, Gray HB, Winkler JR, Wolynes PG. Electrostatic effects on funneled landscapes and structural diversity in denatured protein ensembles Proc. Natl Acad Sci USA. 2009; 106:1796–1801.
2. Flanagan, J Kataoka; Shortle, D.; Engelman, D. Truncated staphylococcal nuclease is compact but disordered. Proc Natl Acad Sci USA. 1992; 89:748–752. [PubMed: 1731350]
3. Flanagan J, Kataoka M, Fujisawa, Engelman D. Mutations can cause large changes in the conformation of a denatured protein. Biochemistry. 1993; 32:10359–10370. [PubMed: 8399179]
4. Sosnick T, Trewhella J. Denatured states of ribonuclease A have compact dimensions and residual secondary structure. Biochemistry. 1992; 31:8329–8335. [PubMed: 1525171]
5. Segel DJ, Fink AL, Hodgson KO, Doniach S. Protein denaturation: A small-angle X-ray scattering study of the ensemble of unfolded states of cytochrome c. Biochemistry. 1998; 31:12443–12451. [PubMed: 9730816]

Author Manuscript Author Manuscript Author Manuscript Author Manuscript

6. Akiyama S, et al. Conformational landscape of cytochrome c folding studied by microsecond-resolved small-angle X-ray scattering. Proc Natl Acad Sci USA. 2002; 99:1329–1334. [PubMed: 11773620]
7. Pletneva EV, Gray HB, Winkler JR. Snapshots of cytochrome c folding. Proc Natl Acad Sci USA. 2005; 102:18397–18402. [PubMed: 16344477]
8. Pletneva EV, Gray HB, Winkler JR. Nature of the cytochrome c molten globule. J Am Chem Soc. 2005; 127:15370–15371. [PubMed: 16262391]
9. Pletneva EV, Gray HB, Winkler JR. Many faces of the unfolded state: Conformational heterogeneity in denatured yeast cytochrome c. J Mol Biol. 2005; 345:855–867. [PubMed: 15588831]
10. Stigter D, Alonso D, Dill K. Protein stability – electrostatics and compact denatured states. Proc Natl Acad Sci USA. 1991; 88:4176–4180. [PubMed: 2034662]
11. Lattman E, Fiebig K, Dill K. Modeling compact denatured states of proteins. Biochemistry. 1994; 33:6158–6166. [PubMed: 8193129]
12. Chahine J, Nymeyer H, Leite VBP, Socci ND, Onuchic JN. Specific and nonspecific collapse in protein folding funnels. Phys Rev Lett. 2002; 88:168101. [PubMed: 11955268]
13. Levy Y, Wolynes PG, Onuchic JN. Protein topology determines binding mechanism. Proc Natl Acad Sci USA. 2004; 101:511–516. [PubMed: 14694192]
14. Jackson SE. How do small single-domain proteins fold? Fold Des. 1998; 3(4):R81–R91. [PubMed: 9710577]
15. Baldwin RL, Rose GD. Is protein folding hierarchic? II Folding intermediates and transition states. Trends Biochem Sci. 1999; 24(5):77. [PubMed: 10098403]
16. Eaton WA, Munoz V, Hagen SJ, Jas GS, Lapidus LJ, Henry ER, Hofrichter J. Mechanisms in protein folding. Annu Rev Biophys Biomol Structure. 2000; 29:327.
17. Fersht AR. A kinetically significant intermediate in the folding of barnase. Proc Natl Acad Sci USA. 2000; 97:14121–14126. [PubMed: 11114199]
18. Finkelstein AV, Balzitskaya OV. Physics of protein folding Phys. Life Rev. 2004; 1(1):23–56.
19. Kamagata K, Arai M, Kuwajima K. Unification of the folding mechanism of non-two-state and two-state proteins. J Mol Biol. 2004; 343(1):279–279.
20. Ivankov DN, Finkelstein AV. Prediction of protein folding rates from the amino acid sequence-predicted secondary structure Proc. Natl Acad Sci USA. 2004; 101(24):8942–8944.
21. Maity H, Maity M, Krishna MMG, Mayne L, Englander SW. Protein folding: the stepwise assembly of foldon units. Proc Natl Acad Sci USA. 2005; 101(24):4741–4746. [PubMed: 15774579]
22. Feng H, Zhou Z, Bai Y. A protein folding pathway with multiple folding intermediates at atomic resolution Proc. Natl Acad Sci USA. 2005; 102:5026–5031.
23. Lazaridis T, Karplus M. “New view” of protein folding reconciled with the old through multiple unfolding simulations. Science. 1997; 278:1928–1931. [PubMed: 9395391]
24. LaRosa C, Milardi D, Grasso D, Guzzi R, Sportelli L. Thermodynamics of the thermal unfolding of azurin. J Phys Chem. 1995; 99:14864–14870.
25. Guzzi R, LaRosa C, Grasso D, Milardi D, Sportelli L. Experimental model for the thermal denaturation of azurin: A kinetic study. Biophys Chem. 1996; 60:29–38.
26. Rizzuti B, Daggett V, Guzzi R, Sportelli L. The early steps in the unfolding of azurin. Biochemistry. 2004; 43:15604–15609. [PubMed: 15581373]
27. Rizzuti B, Swart M, Sportelli L, Guzzi R. Active site modeling in copper azurin molecular dynamics simulations. J Mol Model. 2004; 10(1):25–31. [PubMed: 14691672]
28. Manetto GD, Grasso DM, Milardi D, Pappalardo M, Guzzi R, Sportelli L, Verbeet MP, Canters GW, LaRosa C. The role played by the cc-helix in the unfolding pathway and stability of azurin: Switching between hierarchic and nonhierarchic folding. ChemBioChem. 2007; 8(16):1941–1949. [PubMed: 17868155]
29. Krishna MMG, Maity H, Rumbley JN, Lin Y, Englander SW. Order of steps in the cytochrome c folding pathway: Evidence for a sequential stabilization mechanism. J Mol Biol. 2006; 359:1410–1419. [PubMed: 16690080]

Author Manuscript Author Manuscript Author Manuscript Author Manuscript

30. Michel LV, Bren KL. Submolecular unfolding unit of Pseudomonas aeruginosa cytochrome c-551. J Biol Inorg Chem. 2008; 13(5):837–845. [PubMed: 18392863]
31. Ramachandran GN, Ramakrishnan C, Sasisekharan V. Stereochemistry of polypeptide chain configurations. J Mol Biol. 1963; 7:95–99. [PubMed: 13990617]
32. Warren JJ, Gray HB, Kozak JJ. A Euclidean perspective on the unfolding of azurin: spatial correlations. J Mol Biol. 2013; 7:95–99.
33. Warren JJ, Gray HB, Winkler JR, Kozak JJ. Euclidean perspective on the unfolding of azurin: angular correlations. Mol Phys. 2013; 111:3762–3769.
34. Gray HB, Warren JJ, Winkler JR, Kozak JJ. A Euclidean perspective on the unfolding of azurin: chain motion. J Biol Inorg Chem. 2014; 19:555–563. [PubMed: 24378983]
35. Lee JC, Engman KC, Tezcan FA, Gray HB, Winkler JR. Structural features of cytochrome c′ folding intermediates revealed by fluorescence energy transfer kinetics. Proc Natl Acad Sci USA. 2002; 99:14778–14782. [PubMed: 12407175]
36. Faraone-Mennella J, Tezcan FA, Gray HB, Winkler JR. Stability and folding kinetics of structurally characterized cytochrome c-b_{562}. Biochemistry. 2006; 45:10504–10511. [PubMed: 16939202]
37. Louie GV, Brayer GD. High-resolution refinement of yeast iso-1-cyrochrome c and comparison with other eukaryotic cytochromes c. J Mol Biol. 1990; 214:527–555. [PubMed: 2166169]
38. Urie KG, Pletneva E, Gray HB, Winkler JR, Kozak JJ. Geometrical analysis of cytochrome c unfolding. Mol Phys. 2011; 109:301–313. [PubMed: 21379364]
39. Gray HB, Winkler JR, Kozak JJ. Unfolding four-helix bundles. Mol Phys. 2011; 109:905–916.
40. Gray HB, Winkler JR, Kozak JJ. Signatures of unfolding in the early stages of protein denaturation. Mol Phys. 2012; 110:419–429.
41. Maity G, Maity M, Englander SW. How cytochrome c folds, and why: submolecular foldon units and their stepwise sequential stabilization. J Mol Biol. 2004; 343:229–233.

Appendices

Table A1(a)

Unfolding of cyt c′ described by averages $\widehat{\langle \lambda_i \rangle}$ for stages n=5 to n=15. In the parenthesis below each entry is the factor which scales the λ_i such that all α-carbon to α-carbon distances between adjacent residues in that segment is 3.80 Å.

Segment	Region	n=5	n=7	n=9	n=11	n=13	n=15	Turns
3–26	**H-1**	**1.22 (0.94)**	**1.18 (0.99)**	**1.21 (0.97)**	**1.27 (0.89)**	**1.20 (0.95)**	**1.16 (0.96)**	**6**
33–60	**H-2**	**1.15 (0.85)**	**1.03 (0.97)**	**1.03 (0.97)**	**1.10 (0.91)**	**1.05 (0.92)**	**1.09 (0.88)**	**7**
61–67	**K**	**1.17 (0.83)**	**1.22 (0.78)**	**1.33 (0.67)**	**1.09 (0.91)**	**1.39 (0.61)**	**1.22 (0.78)**	
68–96	**H3**	**1.26 (0.74)**	**1.02 (0.98)**	**1.05 (0.95)**	**1.24 (0.76)**	**1.16 (0.94)**	**1.07 (0.93)**	**7**
100–121	**H4**	**1.22 (0.78)**	**1.01 (1.00)**	**1.07 (0.93)**	**1.21 (0.75)**	**1.09 (0.91)**	**1.10 (0.90)**	**5**

Table A1(b)

Unfolding of cyt c-b_{562} described by averages $\widehat{\langle \lambda_i \rangle}$ for stages n=5 to n=15. In the parenthesis below each entry is the factor which scales the λ_i such that all α-carbon to α-carbon distances between adjacent residues in that segment is 3.80 Å.

Segment	Region	n=5	n=7	n=9	n=11	n=13	n=15	Turns
3–19	**H-1**	**1.02 (1.00)**	**0.97 (1.05)**	**1.08 (0.95)**	**1.01 (0.92)**	**1.36 (0.72)**	**1.15 (0.85)**	**4**
24–40	**H-2**	**1.03 (0.97)**	**1.00 (1.00)**	**1.04 (0.96)**	**1.14 (0.86)**	**1.15 (0.85)**	**1.18 (0.82)**	**4**

Author Manuscript Author Manuscript Author Manuscript Author Manuscript

Segment	Region	n=5	n=7	n=9	n=11	n=13	n=15	Turns
41–55	**K**	**1.17 (0.83)**	**1.22 (0.78)**	**1.33 (0.67)**	**1.09 (0.91)**	**1.39 (0.61)**	**1.22 (0.78)**	
56–80	**H3**	**1.02 (0.98)**	**1.06 (0.94)**	**1.03 (1.03)**	**1.09 (0.91)**	**1.19 (0.81)**	**1.14 (0.86)**	**6**
85–104	**H4**	**1.08 (0.93)**	**1.00 (1.00)**	**0.97 (1.04)**	**1.06 (0.94)**	**1.21 (0.79)**	**1.12 (0.88)**	**5**

Table A1(c)

Unfolding of cyt c described by averages $\langle \lambda_i \rangle$ for stages n=5 to n=15. In the parenthesis below each entry is the factor which scales the λ_i such that all α-carbon to α-carbon distances between adjacent residues in that segment is 3.80 Å.

Segment	Region	n=5	n=7	n=9	n=11	n=13	n=15
3–14	**Blue Helix 1**	1.43 (0.81)	1.27 (0.99)	1.28 (1.01)	1.24 (1.07)	1.31 (0.98)	1.17 (1.06)
19–36	**Green Loop**	1.33 (0.67)	1.27 (0.73)	1.30 (0.70)	1.26 (0.74)	1.27 (0.73)	1.22 (0.78)
40–57	**Infrared Loop**	1.19 (0.85)	1.23 (0.77)	1.21 (0.79)	1.05 (0.95)	1.20 (0.65)	1.04 (0.89)
62–70	**Green Helix**	1.33 (0.67)	1.02 (0.98)	1.14 (0.86)	1.26 (0.73)	1.23 (0.77)	0.96 (1.04)
71–85	**Red Loop**	1.20 (0.80)	1.09 (0.91)	1.10 (0.90)	1.18 (0.83)	1.25 (0.75)	1.34 (0.66)
87–101	**Blue Helix 2**	1.13 (0.87)	1.09 (0.78)	1.04 (0.96)	1.21 (0.80)	0.88 (1.12)	0.98 (1.02)

Table A2(a)

Unfolding of cyt c′ described by angular averages $\langle \beta_n \rangle$ for unfolding stages n=5 to n=15. In parenthesis below each entry is the angle between terminal residues in the native state.

Segment	Region	n=5	n=7	n=9	n=11	n=13	n=15
3–26	**H-1**	**1.22 (140.5^0)**	**1.80 (142.9^0)**	**2.26 (145.5^0)**	**2.72 (129.6^0)**	**3.36 (124.9^0)**	**3.60 (129.7^0)**
33–60	**H-2**	**1.41 (157.2^0)**	**2.17**	**2.82**	**3.50**	**4.17**	**4.76**
61–67	**K**	**1.66 (12.5^0)**	**1.91**	**2.03**	**2.07**	**2.03**	**2.25**
68–96	**H3**	**1.38 (151.8^0)**	**2.12**	**2.73**	**3.37**	**3.96**	**4.47**
100–121	**H4**	**1.23 (136.5^0)**	**1.89 (124.6^0)**	**2.37 (107.4^0)**	**2.96 (96.2^0)**	**3.26 (98.1^0)**	**3.70 (84.1^0)**

Table A2(b)

Unfolding of cyt c-b_{562} described by angular averages $\langle \beta_n \rangle$ for unfolding stages n=5 to n=15. In parenthesis below each entry is the angle between terminal residues in the native state.

Segment	Region	n=5	n=7	n=9	n=11	n=13	n=15
3–19	**H-1**	**1.10 (112.9^0)**	**1.66 (99.3^0)**	**2.08 (82.3^0)**	**2.56 (78.1^0)**	**2.76 (66.0^0)**	**3.16 (54.1^0)**
24–40	**H-2**	**1.17 (77.1^0)**	**1.92**	**2.42**	**3.11**	**3.84**	**4.47**
41–55	**K**	**1.51 (44.8^0)**	**2.01**	**2.46**	**2.70**	**2.94**	**3.12**
56–80	**H3**	**1.16 (105.7^0)**	**1.84**	**2.31**	**2.87**	**3.47**	**4.01**
85–104	**H4**	**1.51 (119.3^0)**	**2.01 (108.3^0)**	**2.46 (111.3^0)**	**2.70 (97.7^0)**	**2.94 (81.4^0)**	**3.12 (69.4^0)**

Author Manuscript Author Manuscript Author Manuscript Author Manuscript

Table A2(c)

Unfolding of cyt c described by angular averages $\langle \beta_n \rangle$ for unfolding stages n=5 to n=15. In parenthesis below each entry is the angle between terminal residues in the native state.

Segment	Region	n=5	n=7	n=9	n=11	n=13	n=15
3–14	**Blue Helix 1**	1.08 (45.6^0)	1.82 (34.8^0)	2.28 (32.9^0)	2.78 (38.1^0)	2.87 (29.7^0)	3.19 (17.7^0)
19–36	**Green Loop**	1.63 (72.4^0)	2.14	2.30	2.31	2.32	2.65
40–57	**Infrared Loop**	1.70 (20.3^0)	2.26	2.73	3.01	3.32	3.47
62–70	**Green Helix**	1.38 (56.6^0)	2.03	2.41	2.89	3.24	3.34
71–85	**Red Loop**	1.70 (50.0^0)	2.28	2.62	2.77	2.81	2.72
87–101	**Blue Helix 2**	1.38 (80.5^0)	2.17 (71.8^0)	2.96 (67.0^0)	3.65 (64.9^0)	4.67 (57.7^0)	5.74 (49.6^0)

Author Manuscript Author Manuscript Author Manuscript Author Manuscript

HIGHLIGHTS

- We probed the geometrical factors that influence early unfolding in cytochromes.
- Cytochromes c, c′ and c-b562 were our models.
- This permits prediction of unfolding propensities from known structures.

Author Manuscript Author Manuscript Author Manuscript Author Manuscript

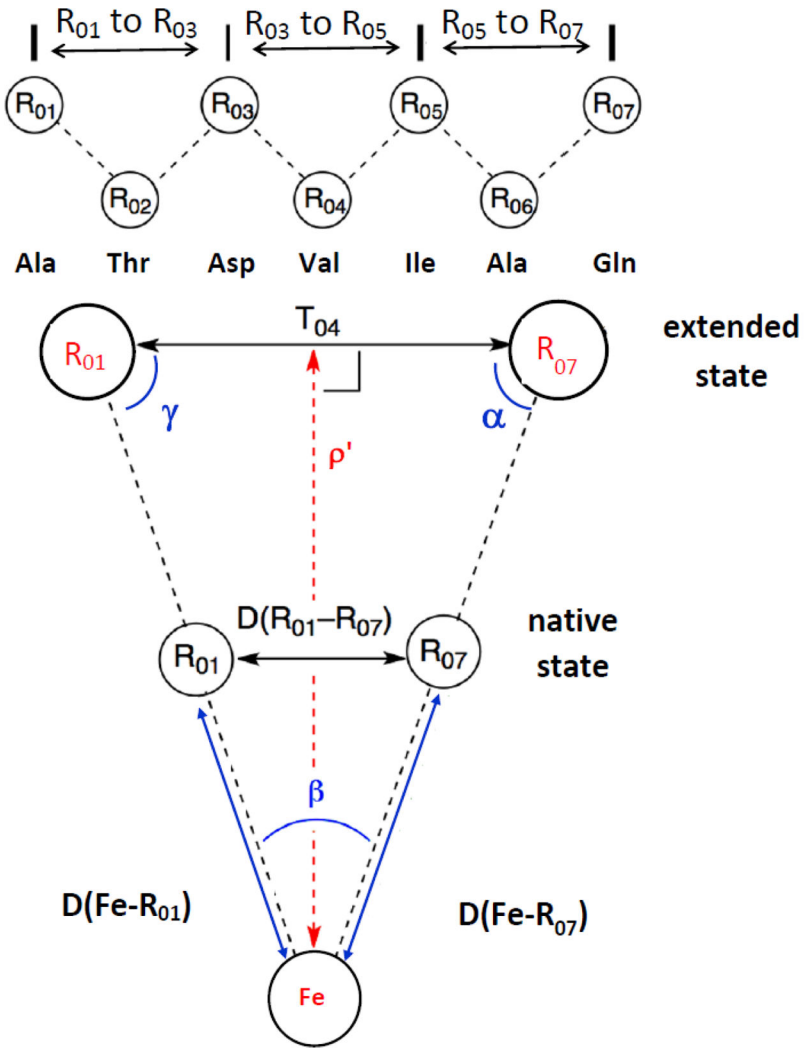

Figure 1.
Specification of the geometrical model for a seven residue segment in cyt c′ (see text).

Author Manuscript Author Manuscript Author Manuscript Author Manuscript

Figure 2a

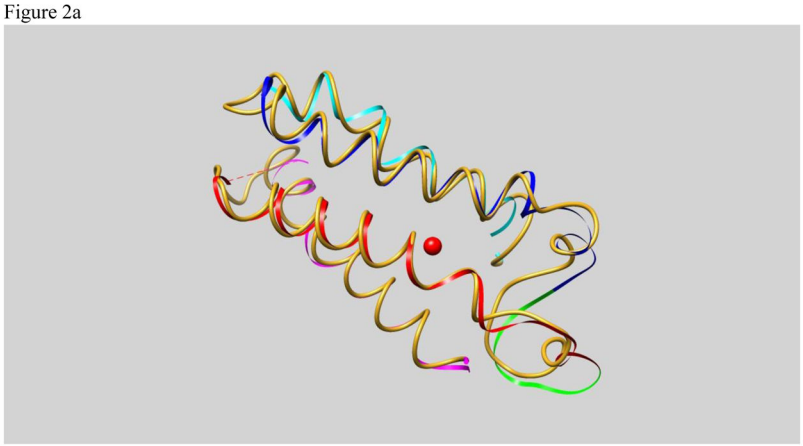

Figure 2b

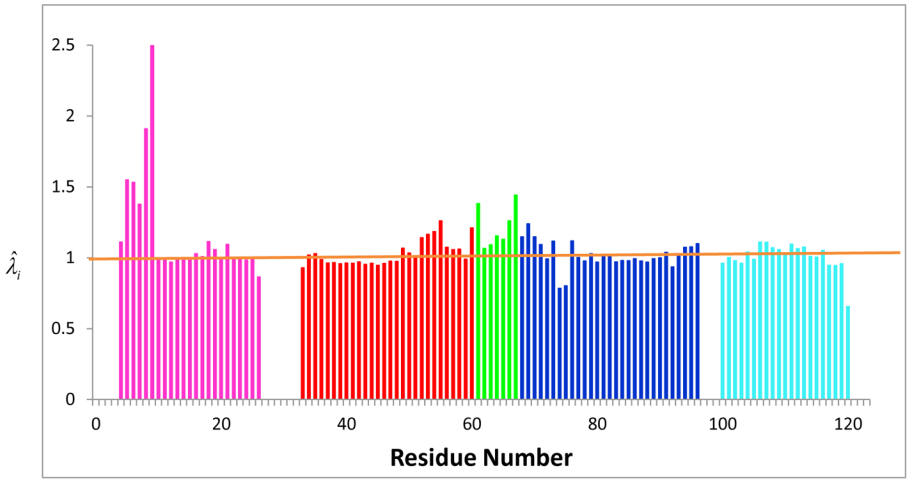

Figure 2.

Figure 2a. Native (goldenrod) and second extended state (n = 7) for cyt *c*′. The N-terminal helix H_1 is coded in magenta, followed by helix H_2 in red, helix H_3 in blue and the C-terminal helix H_4 in cyan. Iron atom is coded in red. The turning region is in green.

Figure 2b. Spatial extension $\hat{\lambda}_i$ relative to the native state (horizontal line) versus residue number for cyt *c*′. The color code is specified in Fig. 2a.

Author Manuscript Author Manuscript Author Manuscript Author Manuscript

Figure 3a

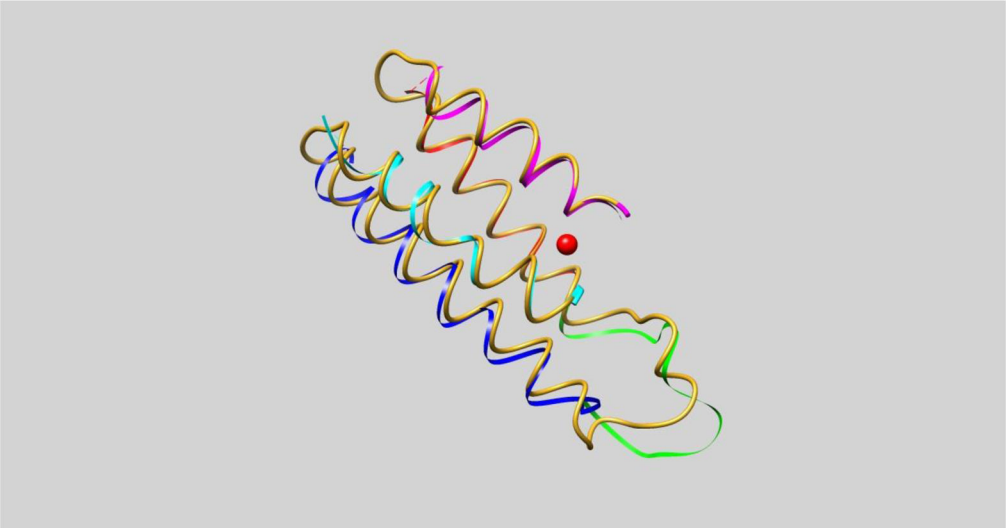

Figure 3b

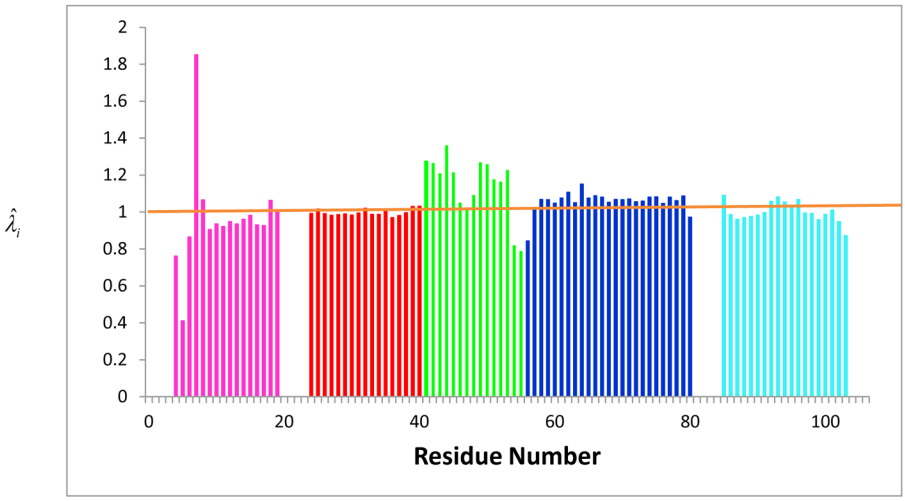

Figure 3.

Figure 3a. Native (goldenrod) and second extended state (n = 7) for cyt *c*-b_{562}. The N-terminal helix H_1 is coded in magenta, followed by helix H_2 in red, helix H_3 in blue and the C-terminal helix H_4 in cyan. Iron atom is coded in red. The turning region is in green.

Figure 3b. Spatial extension $\hat{\lambda}_i$ relative to the native state (horizontal line) versus residue number for cyt *c*-b_{562}. The color code is specified in Fig. 3a.

Author Manuscript Author Manuscript Author Manuscript Author Manuscript

Figure 4a

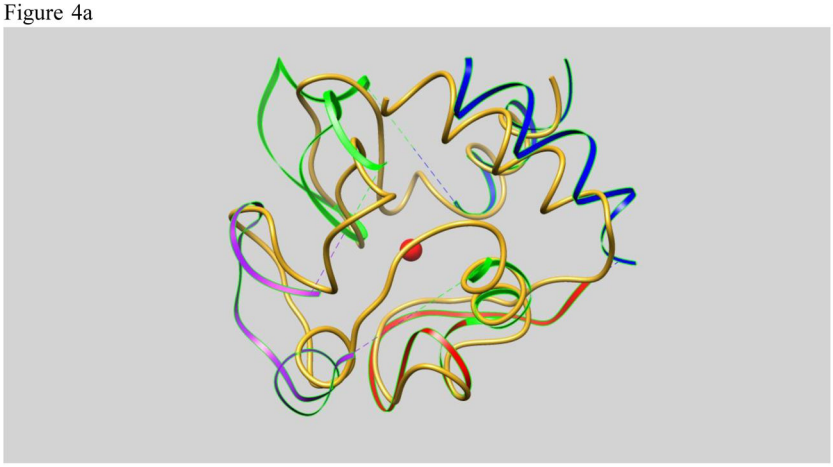

Figure 4b

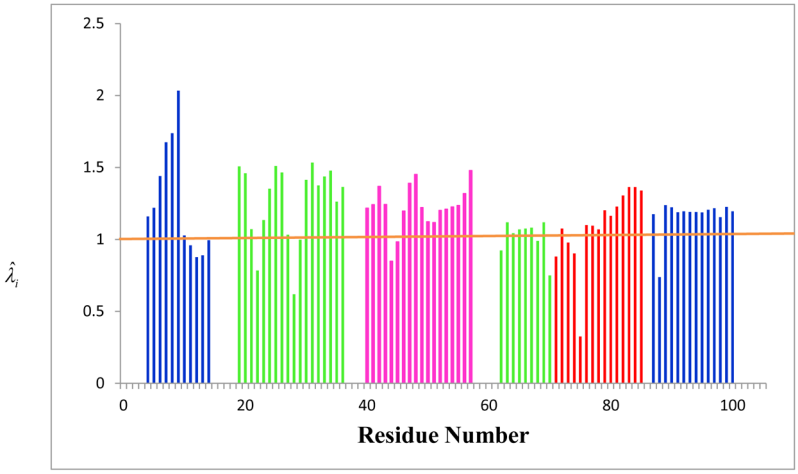

Figure 4c

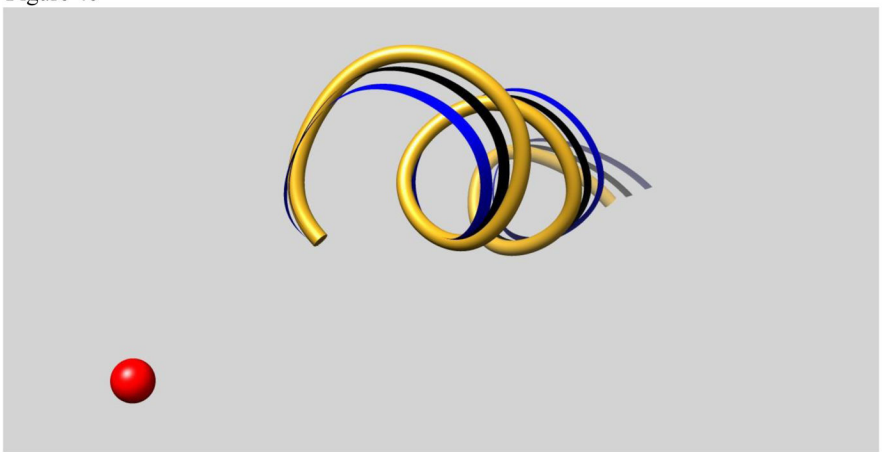

Author Manuscript Author Manuscript Author Manuscript Author Manuscript

Figure 4d

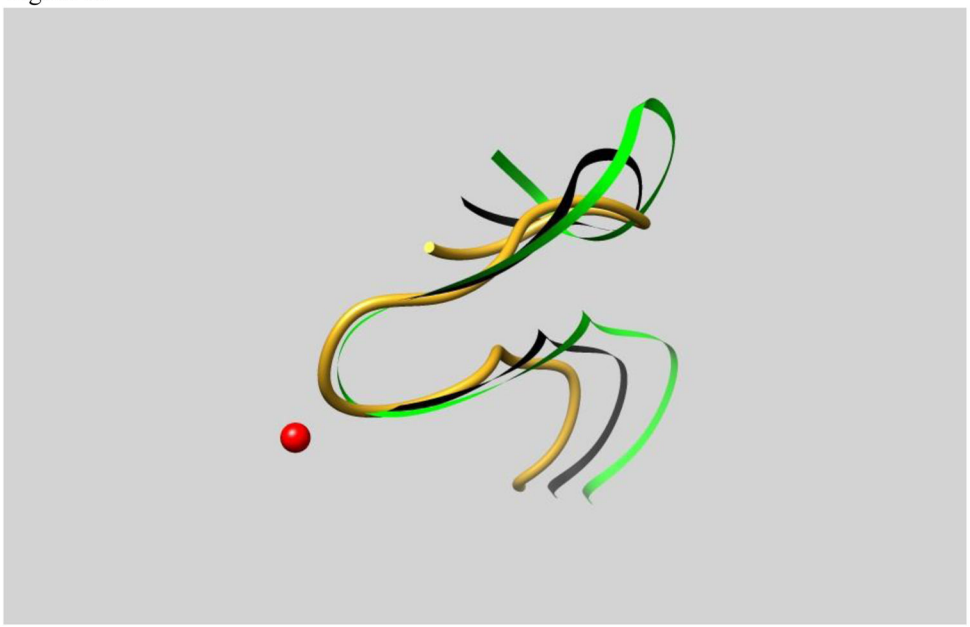

Figure 4e

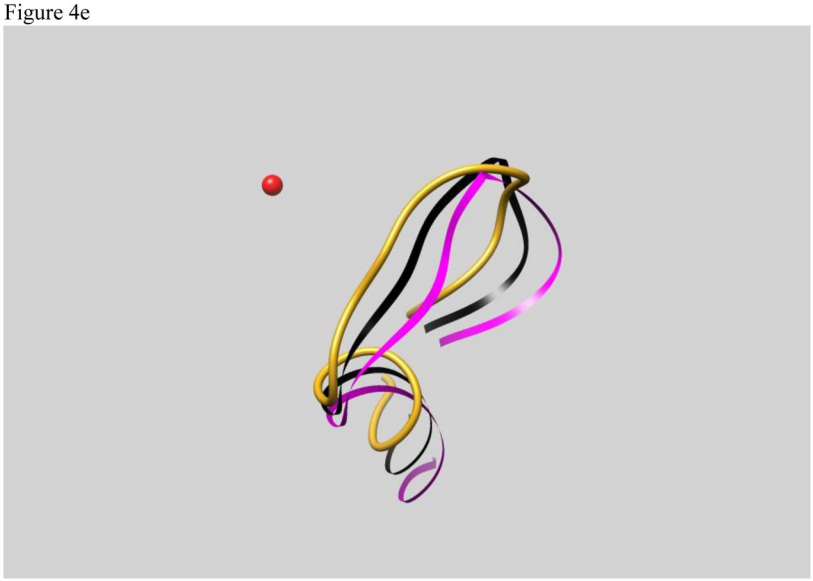

Author Manuscript Author Manuscript Author Manuscript Author Manuscript

Figure 4f

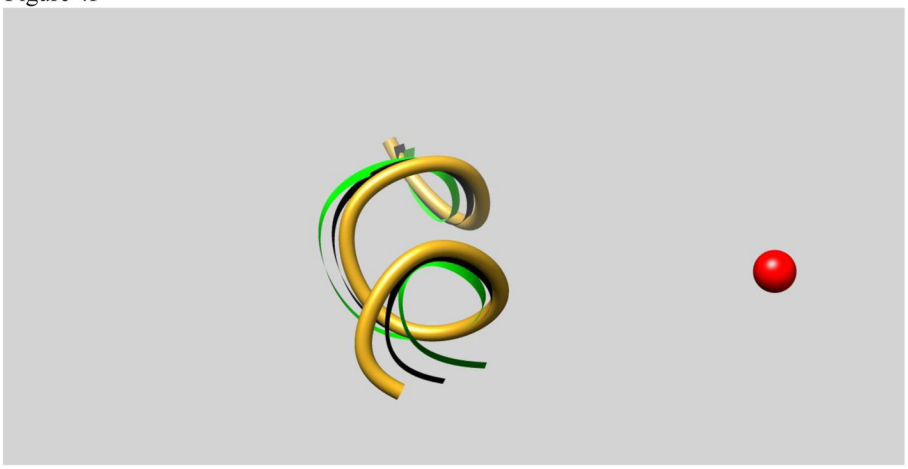

Figure 4g

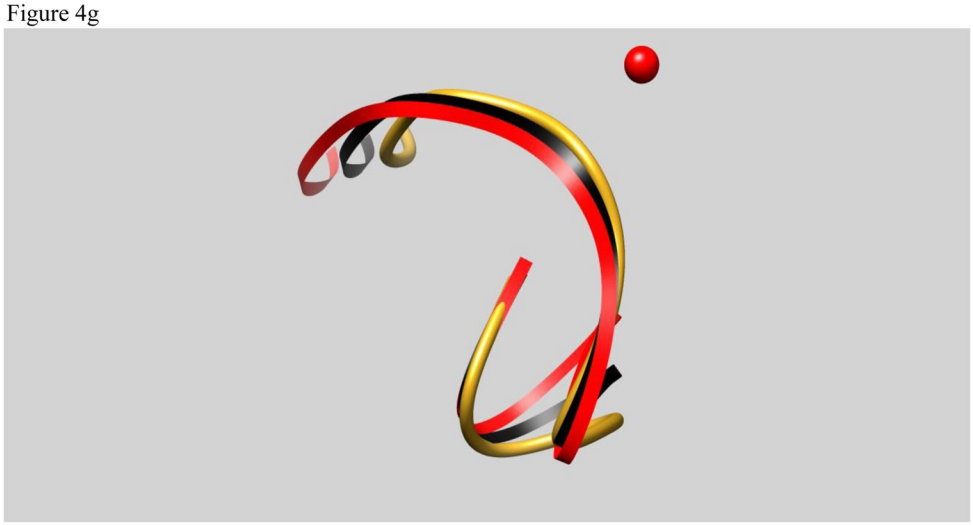

Figure 4h

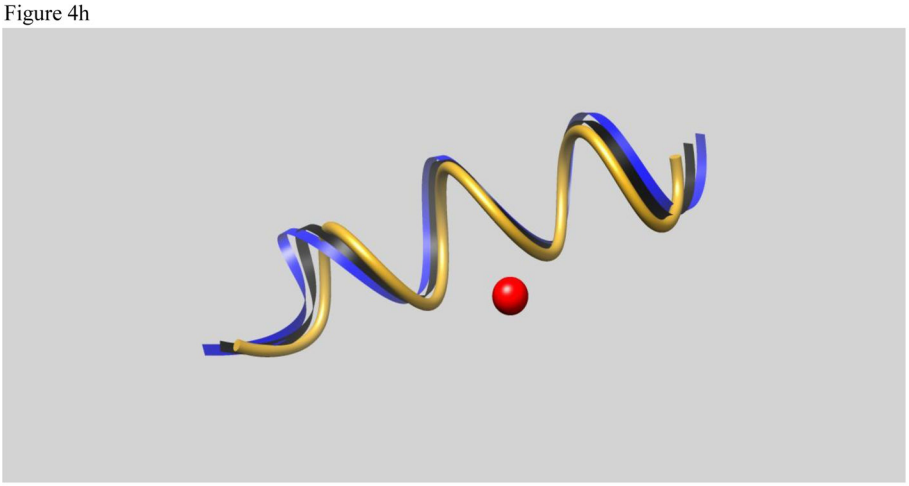

Figure 4.

Author Manuscript Author Manuscript Author Manuscript Author Manuscript

Figure 4a. Native (goldenrod) and second extended state (n = 7) for cyt *c*. We use the color convention for the foldon regions introduced in [41]. The N-terminal and C-terminal α-helices are in blue, the green loop and the green α-helix are in green, the infrared loop is in magenta, and the red loop in red. Iron atom is coded in red.

Figure 4b. Spatial extension $\hat{\lambda_i}$ relative to the native state (horizontal line) versus residue number for cyt *c*. The color code is specified in Fig. 4a.

Figure 4c. Native (goldenrod), first (n = 5) extended state (black) and second (n = 7) extended state (blue) for the N-terminal blue helix in cyt *c*. Iron atom is coded in red.

Figure 4d. Native (goldenrod), first (n = 5) extended state (black) and second (n = 7) extended state (green) for the green loop in cyt c. Iron atom is coded in red.

Figure 4e. Native (goldenrod), first (black) and second extended state (magenta) for the the infrared loop in cyt c. Iron atom is coded in red.

Figure 4f. Native (goldenrod), first (black) and second extended state (green) for the green helix in cyt c. Iron atom is coded in red.

Figure 4g. Native (goldenrod), first (black) and second extended state (red) for the red loop in cyt c. Iron atom is coded in red.

Figure 4h. Native (goldenrod), first (black) and second extended state (blue) for the C-terminal blue helix in cyt c. Iron atom is coded in red.

Author Manuscript Author Manuscript Author Manuscript Author Manuscript

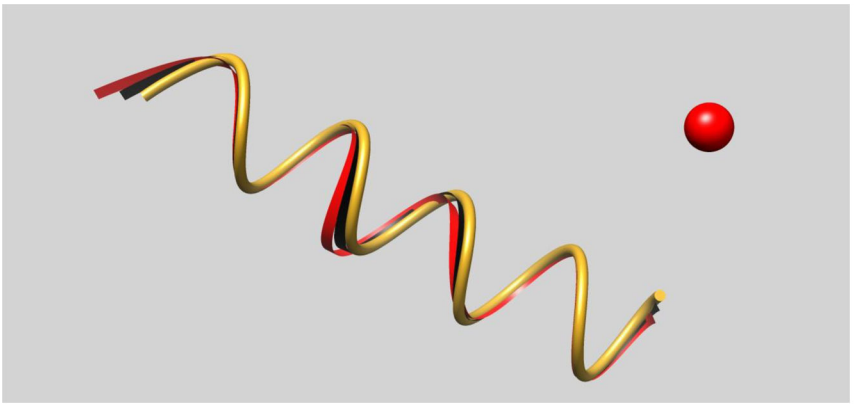

Figure 5.

Native (goldenrod), *first* (n = 5) extended state (black) and *second* (n = 7) extended state (red) for helix H_2 in cyt *c*-b_{562}. Iron atom is coded in red.

Author Manuscript Author Manuscript Author Manuscript Author Manuscript

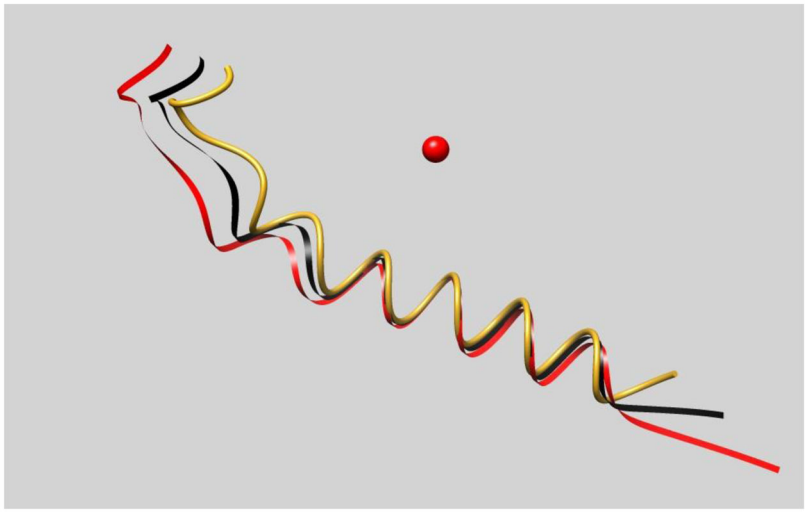

Figure 6.

Native (goldenrod), *first* (n = 5) extended state (black) and *second* (n = 7) extended state (red) for helix H_2 in cyt *c′*. Iron atom is coded in red.

Author Manuscript Author Manuscript Author Manuscript Author Manuscript

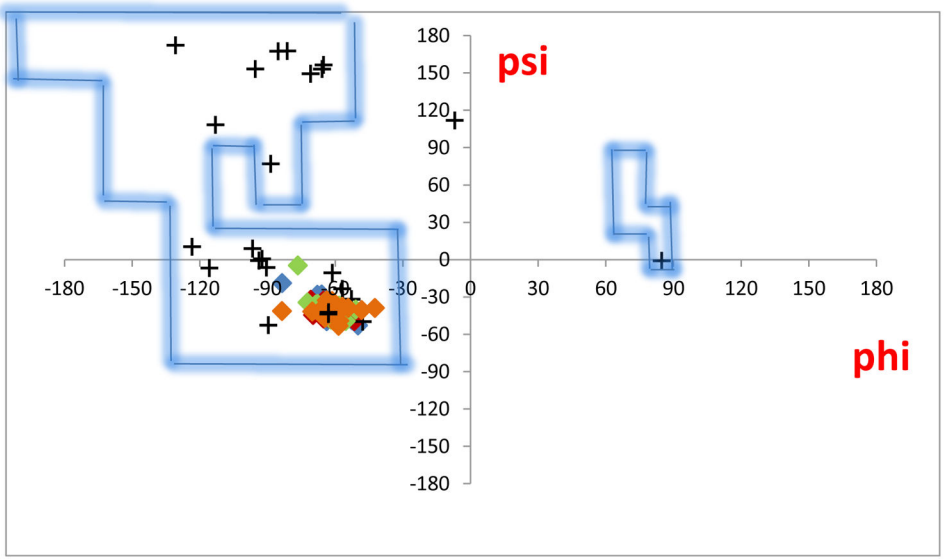

Figure 7.

Phi vs psi for cytochrome cyt *c*-b_{562} where blue diamonds → H_1, red diamonds → H_2, green diamonds → H_3, orange diamonds → H_4 and crosses represent non-helical regions including K.

Author Manuscript Author Manuscript Author Manuscript Author Manuscript

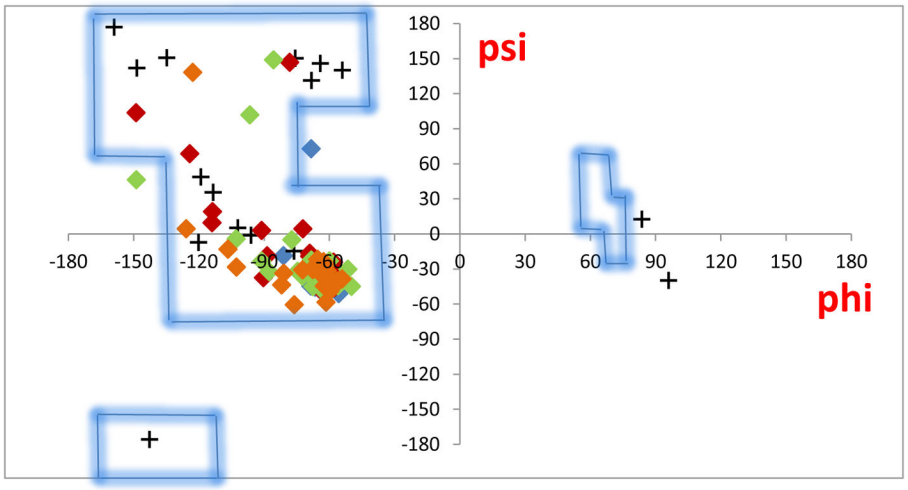

Figure 8.

Phi vs psi for cytochrome c′ where blue diamonds → H_1, red diamonds → H_2, green diamonds → H_3, orange diamonds → H_4 and crosses represent non-helical regions including K.

Author Manuscript Author Manuscript Author Manuscript Author Manuscript

Figure 9a

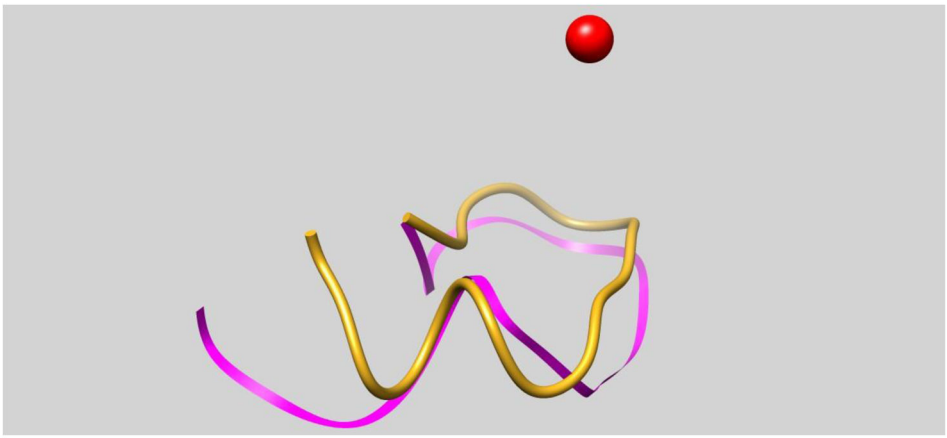

Figure 9b

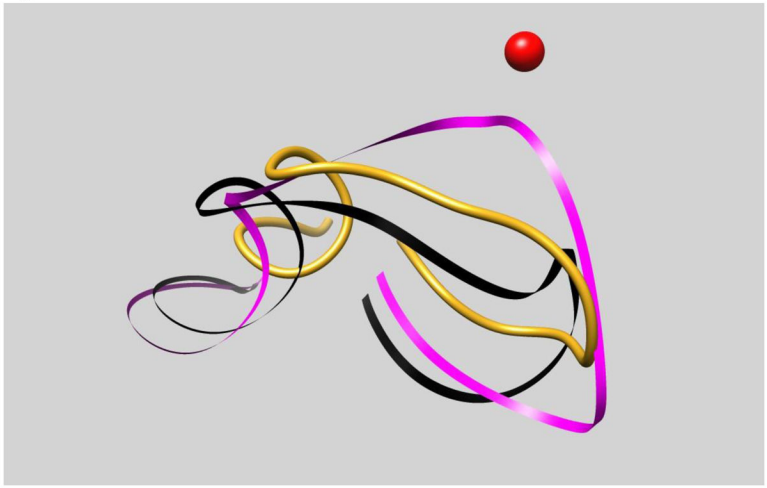

Figure 9.

Figure 9a. Native (goldenrod) and *first* extended state (n = 5) of the infrared (foldon) loop (magenta) in cyt *c*. Iron atom is coded in red.

Figure 9b. Native (goldenrod), *third* extended state (n= 9) (black), and *sixth* extended state (n = 15) of the infrared (foldon) loop (magenta) in cyt c. Iron atom is coded in red.

Author Manuscript Author Manuscript Author Manuscript Author Manuscript

J Inorg Biochem. Author manuscript; available in PMC 2017 February 01.

Table 1

Helical and Turning Regions (K) in Cytochrome *c′*, Cytochrome *c*-b_{562} and Cytochrome *c*[1]

Cytochrome *c′*		Cytochrome *c*-b_{562}		Cytochrome *c*	
Segment	**Region**	**Segment**	**Region**	**Segment**	**Region**
3–26	**Helix 1**	3–19	**Helix 1**	3–14	**Blue Helix 1**
33–60	**Helix 2**	24–40	**Helix 2**	19–36	**Green Loop**
61–67	**K**	41–55	**K**	40–57	**Infrared Loop**
68–96	**Helix 3**	56–80	**Helix 3**	62–70	**Green Helix**
100–121	**Helix 4**	85–104	**Helix 4**	71–85	**Red Loop**
				87–101	**Blue Helix 2**

[1]The PDB ID's of the three cytochromes above are: cytochrome c′ (PDB ID: 1MQV); cytochrome *c*-b_{562} (PDB ID: 2BC5); cytochrome *c* (PDB ID: 1YCC)